AIAA JOURNAL
Vol. 44, No. 5, May 2006

Structure of Three-Dimensional Separated Flow on an Axisymmetric Bump

Gwibo Byun* and Roger L. Simpson†
Virginia Polytechnic Institute and State University, Blacksburg, Virginia 24061

Fine-spatial-resolution laser Doppler velocimeter measurements were obtained on one-half of the leeside of an axisymmetric bump in a turbulent boundary layer. The ratio of bump height H and boundary-layer thickness δ is $H/\delta = 2$. Three-dimensional separations occur on the leeside with one saddle separation on the centerline that is connected with a separation line to one focus separation on each side. Downstream of the saddle point the mean backflow converges to the focal separation points in a region confined within about 0.15δ from the local bump surface. The mean backflow zone is supplied by the intermittent large eddies as well as by the near surface flow from the side of the bump. The separated flow has a higher turbulent kinetic energy and shows bimodal histograms in local U and W, which appear to be due to highly unsteady low-frequency meandering motions. Because of the variation of the mean flow angle in the separation zones, the turbulent flow from different directions is decorrelated, resulting in lower Reynolds shearing stresses. Farther from the wall, large streamwise vortices form from flow around the sides of the bump.

Nomenclature

$A1$	=	structural parameter $\sqrt{[(-\overline{uv})^2 + (-\overline{vw})^2]/(\overline{u^2} + \overline{v^2} + \overline{w^2})}$
H	=	bump height
$\boldsymbol{i}, \boldsymbol{j}, \boldsymbol{k}$	=	unit vectors in the x, y, and z directions, respectively
K	=	kurtosis
$\overline{q^2}$	=	two times turbulent kinetic energy
Re_θ	=	momentum thickness Reynolds number, $U_{\mathrm{ref}}\,\theta/\nu$
R_{uv}	=	correlation coefficient of Reynolds shear stress, $-\overline{uv}/(\sqrt{\overline{u^2}}\sqrt{\overline{v^2}})$
r	=	local radius of bump
S	=	skewness
U, V, W	=	instantaneous velocities in the x, y, and z directions, respectively
$\bar{U}$, $\bar{V}$, $\bar{W}$	=	mean velocities in the x, y, and z directions, respectively
U_{ref}	=	reference freestream velocity
$\overline{uv}$, $\overline{uw}$, $\overline{vw}$	=	Reynolds shearing stresses
$\overline{u^2}$, $\overline{v^2}$, $\overline{w^2}$	=	Reynolds normal stresses
u_τ	=	skin-friction velocity $\sqrt{(\tau_w/\rho)}$
u', v', w'	=	velocity fluctuations in the x, y, and z directions, respectively
$\boldsymbol{V}_q$	=	turbulent kinetic energy transport velocity vector
x	=	streamwise direction in tunnel coordinates
x_L	=	radial direction tangent to bump surface in local coordinates
y	=	vertical direction in tunnel coordinates
y_L	=	vertical direction normal to bump surface in local coordinates
y^+_{L0}	=	nondimensional distance from bump surface normalized by two-dimensional turbulent boundary layer u_τ
z	=	spanwise direction in tunnel coordinates
z_L	=	circumferential direction tangent to bump surface in local coordinates
γ_P	=	time fraction of forward flow
θ	=	momentum thickness, pitch angle
ν	=	kinematic viscosity
τ	=	local shear stress
τ_w	=	local wall shear stress
ψ	=	yaw angle
$1/S$	=	Reynolds stresses ratio, $\sqrt{[(-\overline{uv})^2 + (-\overline{vw})^2]}/\overline{v^2}$

Subscript

L	=	quantities in local coordinate system

I. Introduction

THE turbulent flow separation from a three-dimensional body is still not understood completely due to its complexity, even though it is a quite common phenomenon and plays a important role in practical cases. Most previous investigations of three-dimensional flow separation depend on the surface topological analysis and the critical point (saddle, node, and focus) theory that are based on the flow visualization.[1–3] However, they only can describe the flow structures qualitatively, not quantitatively. Thus, the computational analysis of this kind of flowfield is difficult to model properly without detailed quantitative data. Now computational fluid dynamics (CFD) researchers have extended their challenges to more complex three-dimensional turbulent flowfields.[4] Several CFD research groups have used the flow over the same bump that Simpson et al.[5] examined as a test case to improve their models. Patel et al.[6] studied the axisymmetric bump using large-eddy simulation (LES). They showed multiple separations and reattachments on the leeside of the bump. Wang et al.[7] calculated separated flow from this bump using the Reynolds-averaged Navier–Stokes (RANS) equations with different nonlinear eddy–viscosity (NLEV) models. Temmerman et al.[8] performed a comparative study of separation from this bump by LES and RANS. Davidson and Dahlström[9] have reported their hybrid LES–RANS for the flow around the bump. They used the unsteady RANS near the wall and switched to LES at a specific height from the wall. They obtained the best agreement with experiments at the wake plane at $x/H \approx 3.6$ among all CFD previous results. Although CFD results are qualitatively consistent with experimental

Presented as Paper 2005-0113 at the 43rd Aerospace Sciences Meeting, Reno, NV, 10–13 January 2005; received 6 April 2005; revision received 4 October 2005; accepted for publication 3 November 2005.

*Graduate Research Assistant, Department of Aerospace and Ocean Engineering; currently Senior Research Engineer, Test Team 3, Test Center, Corporate Research and Development Division, Hyundai–Kia Motors, 772-1, Jangduk-Dong, Hwaseong-Si, Gyeonggi-Do 445-706, Republic of Korea. Student Member AIAA.

†Jack E. Cowling Professor, Department of Aerospace and Ocean Engineering, 215 Randolph Hall. President AIAA.

data, a more proper simulation model is necessary. Thus, this research can provide detailed quantitative data for three-dimensional separated turbulent boundary-layer (TBL) flows, which are a good test case to develop better computational models for this type of flowfield.

The present work examines the flow over the axisymmetric, large bump 3, which generates the critical point separations on the leeside of the bump in the TBL. Even though the oilflow, surface pressures, and vorticity flux on the bump surface and the wake plane laser-Doppler velocimeter (LDV) results at $x/H = 3.63$ for this bump have been discussed,[5,10] there is no detailed information of the flow structure of separations and associated physical process on the leeside of bump, where the origin of separations is. Therefore, to capture and examine the structure of separated flow on the leeside of bump, new measurements are reported here using a three-dimensional fiber-optic LDV probe that is placed within the bump with all beams passing through a clear lexan window fit to the curvature of the bump.

II. Experimental Apparatus and Flow Condition

The measurements were conducted in the Virginia Polytechnic Institute and State University (VPI&SU) Aerospace and Ocean Engineering (AOE) Department Low-Speed Boundary Layer Wind Tunnel, which has been used in much previous work. At a nominal speed of $U_{\text{ref}} = 27.5$ m/s and temperature of $25 \pm 1^\circ$C, the turbulence intensity observed in the tunnel freestream was 0.1%, and the potential core was uniform to within 0.5% in the spanwise and 1% in the vertical directions. When the bump was not in place, a mean two-dimensional zero pressure gradient TBL δ, 39 mm thick, was present with $Re_\theta = 7.3 \times 10^3$. The bump was mounted in the floor center of the 0.91-m-wide, 0.25-m-high, and 7.62-m-long test section 3 m from the test section leading edge. It was machined with the axisymmetric shape shown in Fig. 1 that is defined by Eq (1):

$$\frac{y(r)}{H} = -\frac{1}{6.04844}\left[J_0(\Lambda)I_0\left(\Lambda\frac{r}{a}\right) - I_0(\Lambda)J_0\left(\Lambda\frac{r}{a}\right)\right] \qquad (1)$$

where $\Lambda = 3.1962$. For large bump 3, $H = 78$ mm $= 2\delta$ is the height of the bump and $2H$ is the radius of the circular base of the bump. Here, J_0 is the Bessel function of the first kind and I_0 is modified Bessel function of the first kind.

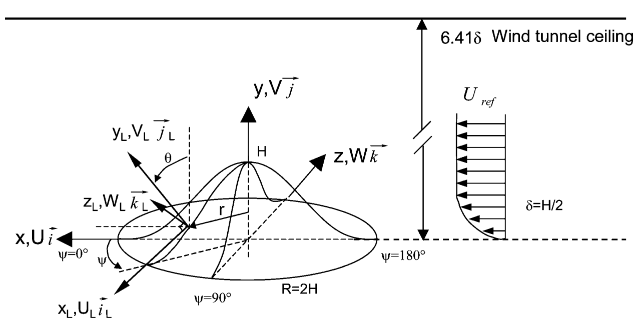

a) Tunnel coordinates, x, y, z; local coordinates, x_L, y_L, z_L; pitch angle θ; and yaw angle ψ

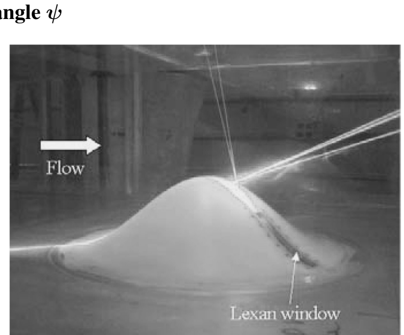

b) Bump with lexan window and five laser beams in dark laboratory

Fig. 1 Schematic and photograph of bump in wind tunnel.

III. Laser-Doppler System

From previous investigations of three different bumps,[10] the large bump 3 is a typical case of three-dimensional vortical separations. To understand these complicated separation patterns it is necessary to measure the flowfield around the bump, including the regions near the wall, especially in the vicinity of the separation, because the oilflow results are affected by flow unsteadiness, oil thickness, and gravity and cannot produce detailed reliable quantitative data.[11] The novel, subminiature LDV system[12] allows these measurements.

The three-velocity-component subminiature LDV probe (miniLDV) is $91.4 \times 25.4 \times 8.9$ mm in size. It has an approximately 78-μm optical measuring volume diameter and an approximately 50-μm coincident effective measuring volume diameter that can be located up to 25 mm from the wall. It is mounted inside the bump, which is on the rotating turret plate. The bump and the probe rotate together about y axis (yaw angle ψ) so that the entire flowfield around the bump can be measured. The 17.8-mm-wide and 0.25-mm-thick antireflection coated transparent lexan window (Fig. 1b), through which laser beams pass, is mounted on the center plane of the bump between $x/H = -0.65$ and 1.8. This window was formed with the curvatures of the bump. There is another rotation stage to rotate only the probe about the z_L axis (pitch angle θ) to locate the probe normal to the window at each measuring point. Hence, it is necessary to transform coordinates from the right-handed local coordinate, x_L, y_L, or z_L, to the right-handed tunnel coordinate, x, y, or z, with θ and ψ. Details of the probe head and the optical components were described by Byun et al.[12] including two-dimensional TBL measurements.

The miniLDV was used in the nearer wall region within about 1 cm from the bump surface. In the outer region, the long LDV system, which is described well by Ölçmen et al.,[13] and the same configuration for the wake plane measurements[5,10] was used. It has about a 88-μm measurement volume diameter that can be located up to 16 cm from the wall.

The Doppler frequency signals are obtained using a National Instruments LabView personal-computer-based three-velocity-component LDV signal processor for miniLDV data and Macrodyne 3100 frequency domain processors for long LDV system data. The data validation percentage from the frequency domain processors was at least 95%, which resulted in minimally noisy data. One block of 15,000 samples over several minutes was taken for each measurement point. The sample rate varied from 20 samples/s very near the wall to 200–300 samples/s away from the wall. The aerosol seeding system[14] used dioctal phthalate (DOP) with a measured mean particle size of about 0.7 μm. The outlying data points from histograms were removed in the LDV optics coordinate system as well as after rotation into the local coordinate system, as described by Ölçmen and Simpson.[14] Because there was no correlation between the data rate fluctuation and the velocity magnitude fluctuation, no velocity bias correction was applied. Velocity gradient broadening, finite transit time and instrument broadening of the signals were also negligible.

The uncertainty was calculated using two acquired data sets and Chauvenet's criterion to calculate the standard deviation σ

$$d_{\max}/\sigma = 1.15 \qquad (2)$$

where $d_{\max}$ is the average of one-half of the differences between two data values for each quantity. The 20:1 odds uncertainties were calculated as $\pm 1.96\sigma$ in Table 1.

IV. Results and Discussion

Measurements have been performed over one-half of the bump leeside at various yaw ψ and pitch θ angles. The yaw angle changes by 10 deg for $0 \le \psi \le 90$ deg and by 30 deg for $90 < \psi \le 180$ deg. The miniLDV probe volume was traversed perpendicularly from the bump surface between about $y_L \approx 100$ μm and $y_L \approx 1$ cm, where $y^+_{L0} \approx 6$–578 based on two-dimensional $u_\tau = 0.96$ at the center location of bump. The long LDV system was used for farther locations. Because of detailed measurements only on one-half of the leeside, it was necessary to check the mean flow symmetry over the bump.

Table 1 Uncertainties in measured quantities in 20:1 odds

Quantity	Uncertainty
$\bar{U}/U_{\mathrm{ref}}$	±0.0096
$\bar{V}/U_{\mathrm{ref}}$	±0.0046
$\bar{W}/U_{\mathrm{ref}}$	±0.0037
$\overline{u^2}/U^2_{\mathrm{ref}}$	±0.00098
$\overline{v^2}/U^2_{\mathrm{ref}}$	±0.00034
$\overline{w^2}/U^2_{\mathrm{ref}}$	±0.00069
$\overline{uv}/U^2_{\mathrm{ref}}$	±0.00038
$\overline{uw}/U^2_{\mathrm{ref}}$	±0.00052
$\overline{vw}/U^2_{\mathrm{ref}}$	±0.00024
$\overline{u^2v}/U^3_{\mathrm{ref}}$	±0.000066
$\overline{u^2w}/U^3_{\mathrm{ref}}$	±0.000051
$\overline{v^2w}/U^3_{\mathrm{ref}}$	±0.000022
$\overline{uv^2}/U^3_{\mathrm{ref}}$	±0.000043
$\overline{uw^2}/U^3_{\mathrm{ref}}$	±0.00004
$\overline{vw^2}/U^3_{\mathrm{ref}}$	±0.000024
$\overline{uvw}/U^3_{\mathrm{ref}}$	±0.000023
$\overline{u^3}/U^3_{\mathrm{ref}}$	±0.00013
$\overline{v^3}/U^3_{\mathrm{ref}}$	±0.000038
$\overline{w^3}/U^3_{\mathrm{ref}}$	±0.000043

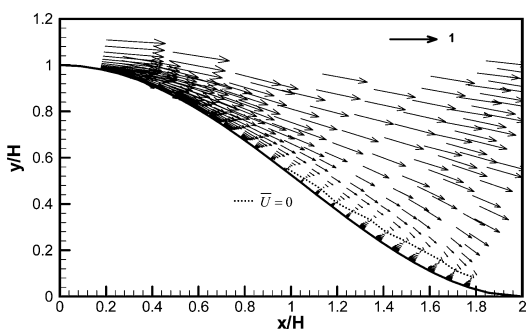

Fig. 2 Normalized $Ui + Vj$ vectors in the center plane: · · · ·, $\bar{U} = 0$.

Although not presented here, at $r/H = 1.112$ and $y_L = 4$ mm away from the wall, the mean velocities, Reynolds stresses, and triple products within $\psi = \pm 60$ deg show good symmetry within the experimental uncertainties. Note that the symmetric pressure data are from Ref. 5. All miniLDV data satisfy the realizability conditions.[15] Results presented here are for the leeside, $0 \leq \psi \leq 90$-deg.

Mean Velocity Results

Figure 2 shows $\boldsymbol{Ui}$ and $\boldsymbol{Vj}$ vectors normalized by U_{ref} of the center plane. The flow accelerates past the top region and decelerates near the wall due to the adverse pressure gradient. This decelerated flow reaches the stagnation point at about $x/H \approx 0.96$, even though the location is not exact because the velocity magnitude is small within uncertainties. The large mean backflow region is shown from this point below the dashed line, which indicates locations at $\bar{U} = 0$. The mean streamwise flow from upstream and the backflow from downstream converge toward $x/H \approx 0.96$ and finally move away in the spanwise direction from this point to satisfy the continuity equation. Figure 3 shows the intermittency $(\gamma_{pU})_L$, which is the fraction of time that the flow moves downstream (positive velocity) in local coordinates. Simpson defined quantitatively the detachment location as $\gamma_{pU} = 0.5$ for separating mean two-dimensional TBLs.[16] The instantaneous reverse flow first appears at $r/H = 0.644$ near the wall. For downstream r/H, the time fraction of backflow increases up to 46% at $r/H = 0.91$. There is more than 50% backflow for $r/H \geq 0.976$ and downstream, and the backflow region also increases from the wall farther downstream. The $(\gamma_{pU})_L$ has a minimum of about 0.14 at $r/H = 1.615$. Because $(\gamma_{pU})_L$ is never zero, the large eddies supply the intermittently forward flow in this mean backflow region similar to a two-dimensional separated TBL.[16]

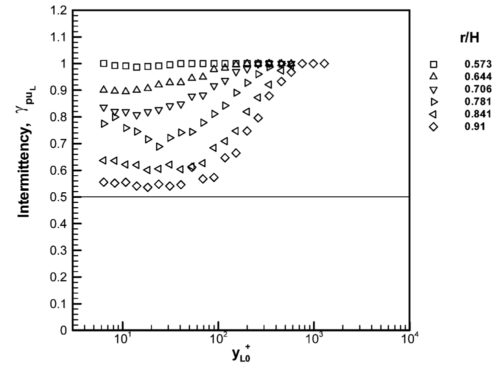

a) Upstream from separation

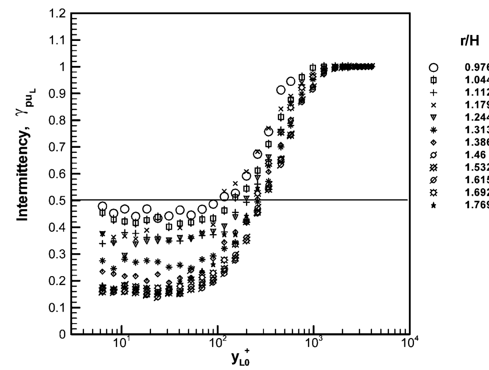

b) Downstream from separation

Fig. 3 Intermittency of U_L in local coordinates along centerline.

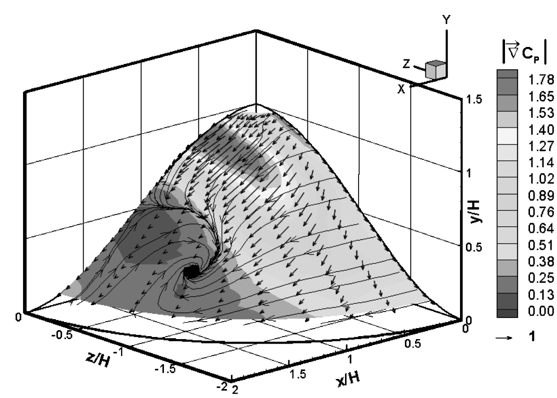

a) Surface pressure gradient contour: - - - -, its vectors and lines connecting $U_L i_L + W_L k_L$ vectors locally tangent to surface at $y^+_{L0} = 11$

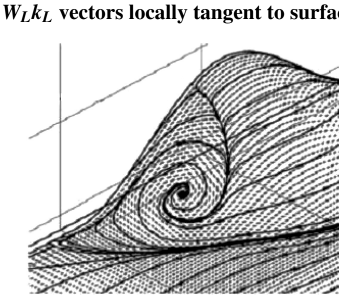

b) Skin-friction lines from quadratic eddy–viscosity model[7]

Fig. 4 Near-wall flowfield.

Figure 4a shows the surface pressure gradient contour, its vectors, and lines connecting tangential velocity vectors of $\boldsymbol{U_L i_L} + \boldsymbol{W_L k_L}$ at $y^+_{L0} = 11$. It shows clearly that the flow converges toward $x/H \approx 0.96$ along the centerline and then moves away in the spanwise direction. If the mirror image is used in the negative z side, this flow pattern is a typical three-dimensional saddle separation. For $|z/H| < 0.8$, the streamwise flow from the upstream and the backflow from the downstream move away from the saddle point

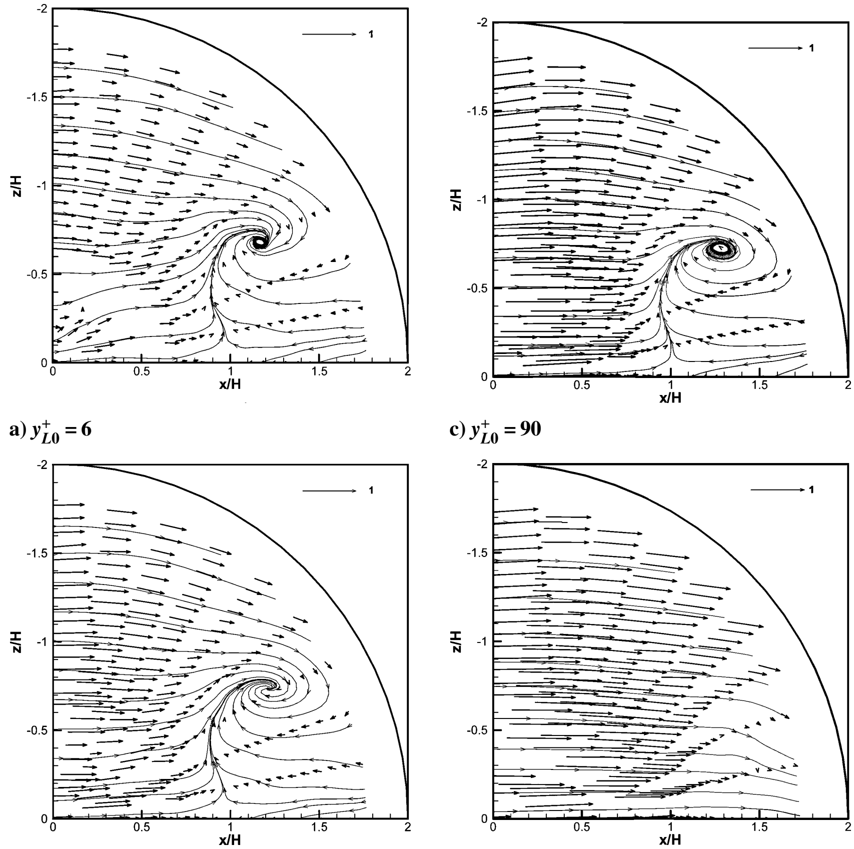

a) $y^+_{L0} = 6$

b) $y^+_{L0} = 24$

c) $y^+_{L0} = 90$

d) $y^+_{L0} = 456$

Fig. 5 Normalized $U_L i_L + W_L k_L$ vectors locally tangent to surface and lines connecting vectors for visual aid only at different y^+_{L0}.

and converge into one trajectory that is the separation line. For $|z/H| > 1$, the streamwise flow from the upstream is deflected toward the centerline due to the spanwise adverse pressure gradient and backflow continuity requirement and is spiraled into the backflow region, $x/H > 1$. Finally, the streamwise flow from the upstream and the backflow from the downstream spiral and converge toward $x/H \approx 1.2$ and $z/H \approx 0.7$. The flow at this point forms a focus separation and satisfies the continuity equation. The separation line from the saddle point ends at the focus. This saddle–foci structure, with another focus on the positive z side because of the symmetric flow, is not only on the nearest surface but is also in the flowfield up to $y^+_{L0} \approx 340$. A separation surface emanates from the separation line and the vortical rolling up from the foci. Delery[1] called this vortical structure a "tornado-like vortex." Because y^+_{L0} increases more, this vortex is not shown in Fig. 5d.

The LDV data show a different near surface flow pattern from the oilflow visualization presented by Byun et al.[10] and Simpson et al.[5] They do not show foci separations between $x/H \approx 0.18$ and 0.4 because there is no backflow in this region. In addition, there is no clockwise focus on the negative z side between $x/H \approx 1$ and 1.5 because of no separation about $x/H \approx 1.5$ and no mean streamwise flow in this region from the LDV data. These differences probably come from the effect of gravity (maximum slope of bump approximately 38 deg), the unsteadiness on the finite thickness oil mixture, and the shear stress of the backflow. Unlike the oilflow visualization, the LDV data show only one focus on each side, which is similar to the oilflow visualization of the small bump 3 with height $H = \delta$ (Ref. 10). Using a quadratic eddy–viscosity model, Wang et al.[7] calculated very similar results for the leeside near-wall region, as shown in Fig. 4b by the skin-friction lines on the positive z/H side. The saddle separation on the centerline is calculated far upstream of the experimentally measured location.

To understand the mean flow structures better, Fig. 6 shows three-dimensional mean streamlines using $\bar{U}$, $\bar{V}$, and $\bar{W}$. Streamlines from a to j start from $x/H = 0.645$, upstream from the saddle separation, at $y/H = 0.781$ and $-0.05 \geq z/H \geq -0.5$ with $\Delta z/H = 0.05$. Note that the y^+_{L0} at the beginning of each streamline increases spanwise as indicated in Fig. 6. Streamline k starts from $x/H = 0.63$, $y/H = 0.549$, and $z/H = -0.751$. Note that they show mean velocity flow patterns, not instantaneous flow features. Streamlines from a to c near the wall, $y^+_{L0} \leq 53$, and close to the centerline, $z/H \leq -0.15$, move spanwise as they approach the saddle separation and separate near $x/H \approx 1$ around the separation line originating from the saddle separation. These separated flow mean streamlines are entrained into the mean backflow region downstream, even though we know from Fig. 3 that the backflow is intermittent and some forward flow is supplied by the large eddies. They spiral toward the focus and then separate. A little farther from the centerline and the surface, mean streamlines d and e, which start from $y^+_{L0} = 91$ and 139 and $z/H = -0.2$ and -0.25, respectively, move almost straight downstream, but they are entrained by large eddies toward the centerline and the surface after $x/H \approx 1.5$. In particular, after the entrainment, streamline d moves backward upstream and spirals toward the focus. Downstream from the saddle separation, the large eddies sweep fluid into the near surface frequently like that for separated two-dimensional mean TBLs.[16] Streamlines from f to j, $y^+_{L0} \geq 197$, roll downstream counterclockwise toward the centerline over the top of mean streamlines from a to e and show the positive streamwise vortices as measured at the wake planes.[5,10] Streamline k, starting farther spanwise from the centerline near the wall, $z/H = -0.751$, and $y^+_{L0} = 31$, moves toward the center downstream and spirals upstream toward the focus. Thus, the mean backflow zone is supplied by the large eddy structure and by flow from the sides of the bump.

Turbulent Kinetic Energy and Correlation Coefficients Related to Reynolds Stresses

Contours of the turbulent kinetic energy (TKE) $\equiv \overline{q^2}/2 = (\overline{u^2} + \overline{v^2} + \overline{w^2}/2)$, normalized by U_{ref} and its transport velocity vectors, $\boldsymbol{V}_q/U_{\text{ref}} \equiv (V_{qu}\boldsymbol{i} + V_{qv}\boldsymbol{j})/U_{\text{ref}} \equiv (\overline{uq^2}\boldsymbol{i} + \overline{vq^2}\boldsymbol{j})/\overline{q^2}U_{\text{ref}}$,

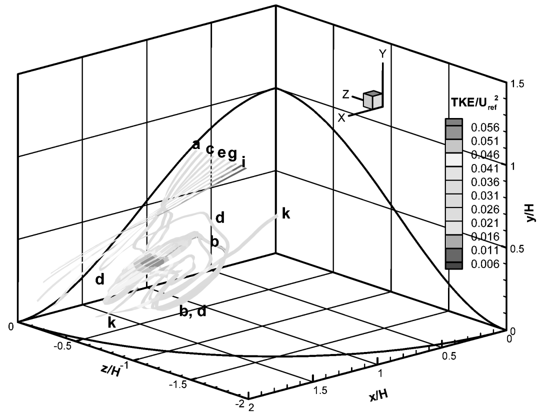

a) Three-dimensional perspective view

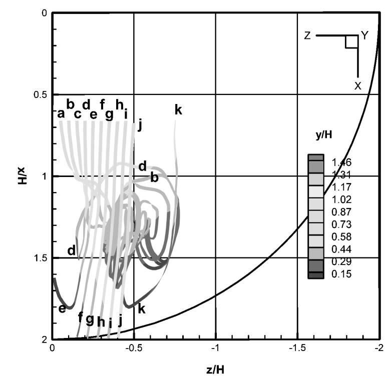

b) View from top

y_{L0}^+	
a	10
b	26
c	53
d	91
e	139
f	197
g	265
h	342
i	429
j	523
k	31

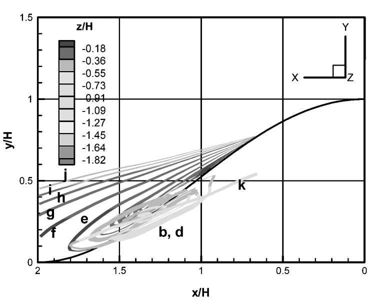

c) View from side

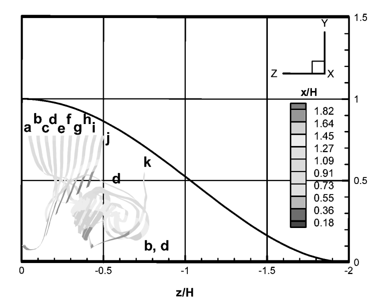

d) View from downstream

Fig. 6 Some three-dimensional streamlines using $\bar{U}$, $\bar{V}$, and $\bar{W}$ from various y_{L0}^+ starting points; contours show TKE levels and out-of-plane positions.

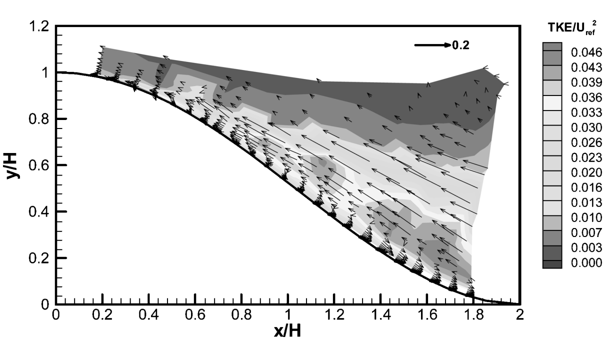

Fig. 7 TKE contour and its normalized transport vectors $V_{qu}\boldsymbol{i} + V_{qv}\boldsymbol{j}$ in center plane.

at the center plane are shown in Fig. 7. For several y_{L0}^+, Fig. 8 shows TKE contours and its transport velocity vector components that are locally parallel to the surface, $\boldsymbol{V}_{qL}/U_{\mathrm{ref}} \equiv (V_{quL}\boldsymbol{i}_L + V_{qwL}\boldsymbol{k}_L)/U_{\mathrm{ref}} \equiv (\overline{u_L q^2}\boldsymbol{i}_L + \overline{w_L q^2}\boldsymbol{k}_L)/\overline{q^2}U_{\mathrm{ref}}$, and lines connecting tangential velocity vectors of $\overline{U_L}\boldsymbol{i}_L + \overline{W_L}\boldsymbol{k}_L$. Near the wall, the high turbulent shear stresses and velocity gradient generate the highest TKE level at approximately $x/H \approx 0.3$ after the apex of the bump. As y_{L0}^+ increases, however, the TKE level in this region decreases because of lower TKE production rates. On the other hand, the separated and backflow region, $x/H > 1$ and $|z/H| < 1$, from the saddle and the focus show a high TKE level due to large production rates.

The TKE transport velocity vectors, $\boldsymbol{V}_{qL}/U_{\mathrm{ref}}$, which are derived from the triple products, show the flow transport velocity vectors of the TKE by the turbulent diffusion. Their large magnitudes show some unsteadiness and jitter of the instantaneous flow. Generally, their directions are approximately opposite to the mean velocity vectors, indicating that occasionally the instantaneous velocity is much lower than the mean velocity. For $x/H > 1$, their magnitudes are lower near the wall than away from the wall becauses as y_{L0}^+ increases, the TKE increases in this region, and the unsteady and occasional jittering motions also increase by the vortical separated flow. These meandering motions are outward from the focus along $\psi = 20$ and 40 deg. However, they are streamwise toward the centerline before the focus and opposite after the focus along $\psi = 30$ deg. Around the bump apex, the magnitudes of TKE transport vectors are very strong and have about the same directions as the mean velocity vectors near the wall. This is due to the very high positive $\overline{u^3}$ generated by turbulent sweeping motions toward the wall under the effects of the adverse pressure gradient and the curvature. As y_{L0}^+ increases, the $\boldsymbol{V}_{qL}/U_{\mathrm{ref}}$ magnitude becomes smaller, and the directions change opposite to the mean velocity vectors because of turbulent ejection motions from the wall. The turbulence intensity $(TI) \equiv \sqrt{[\overline{q^2}/(\overline{U}^2 + \overline{V}^2 + \overline{W}^2)]}$, normalized by local mean velocities, which is not present here, may be a better parameter than TKE normalized by U_{ref} to show the local turbulence level on the leeside of the bump. Near the wall, the TI has a very high level of about 10–18 along the separation line from the saddle point to the focus point because of very low mean velocities. As y_{L0}^+ increases, the high TI zone moves and spreads downstream because of the separated flow, which has higher Reynolds normal stresses as well as low mean velocities.

Figure 9 shows the parameter $1/S \equiv [(-\overline{uv_L})^2 + (-\overline{vw_L})^2]^{0.5}/\overline{v_L^2}$ vs y_{L0}^+ in local coordinates. It is independent of the coordinate rotation about the y_L axis, which is normal to the wall. Because $\overline{v^2}$ contains little contribution from inactive turbulent motions, this parameter is a type of Reynolds stress correlation coefficient. Inactive motions are low-frequency, long-wavelength structures that produce little Reynolds shearing stresses. Note that this parameter is almost constant at about 0.6 for $100 \le y^+ \le 1200$ in a two-dimensional TBL and has a similar behavior for three-dimensional flows as for two-dimensional flows if there are no embedded streamwise vortices.[17] For $r/H < 0.781$, $1/S$ is lower than a two-dimensional TBL below $y_{L0}^+ \approx 100$ within $0 \le \psi \le 40$ deg due to much higher $\overline{v^2}$, in spite of relatively high Reynolds shearing stresses. For $0 \le \psi \le 40$ deg, $1/S$ in the inner layers, $20\text{–}30 \le y_{L0}^+ \le 400\text{–}500$, is much lower than a

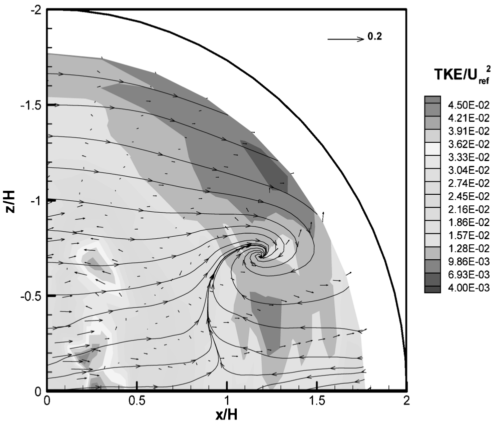

a) $y_{L0}^+ = 11$

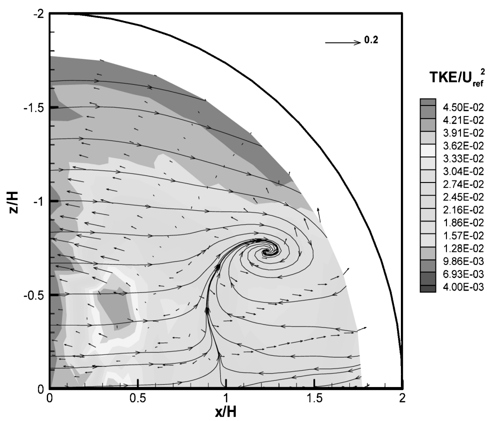

b) $y_{L0}^+ = 41$

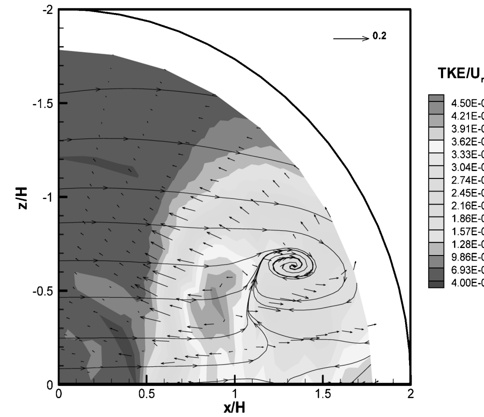

c) $y_{L0}^+ = 200$

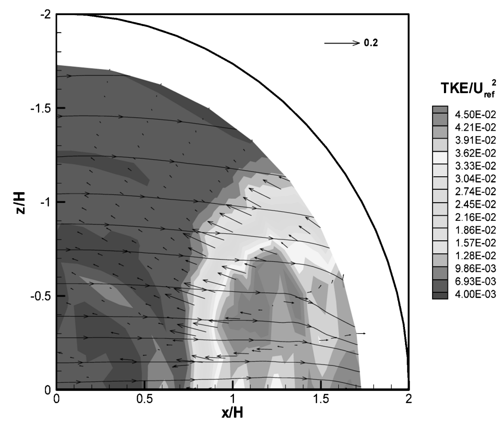

d) $y_{L0}^+ = 456$

Fig. 8 TKE contours, - - - -, and normalized transport vectors $V_{quL} i_L + V_{qwL} K_L$ locally tangent to surface at different y_{L0}^+; from Fig. 5, ——, for visual aid of locally tangential mean velocity directions.

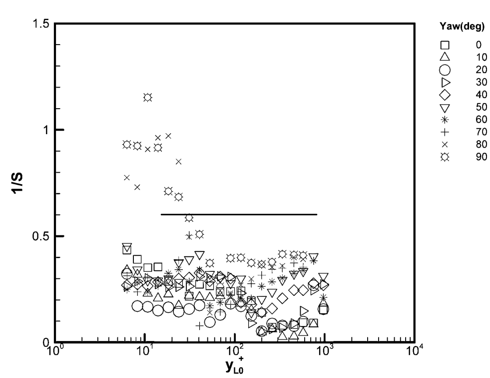

a) $r/H = 0.644$

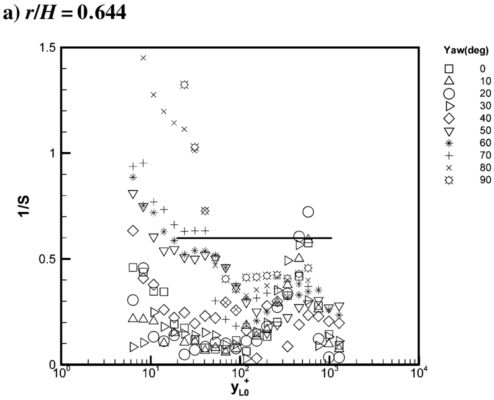

b) $r/H = 0.91$

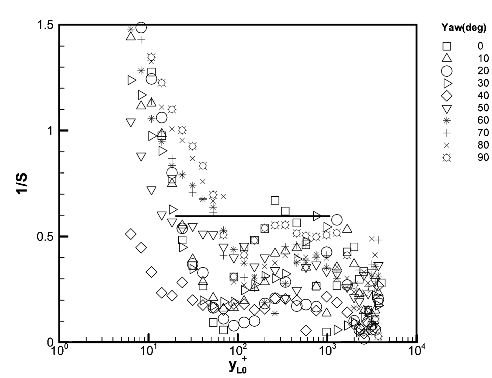

c) $r/H = 1.386$

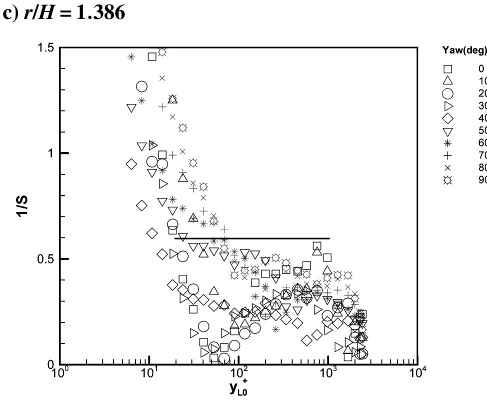

d) $r/H = 1.615$

Fig. 9 1/S parameter in local coordinates: ——, two-dimensional TBL level over middle region.

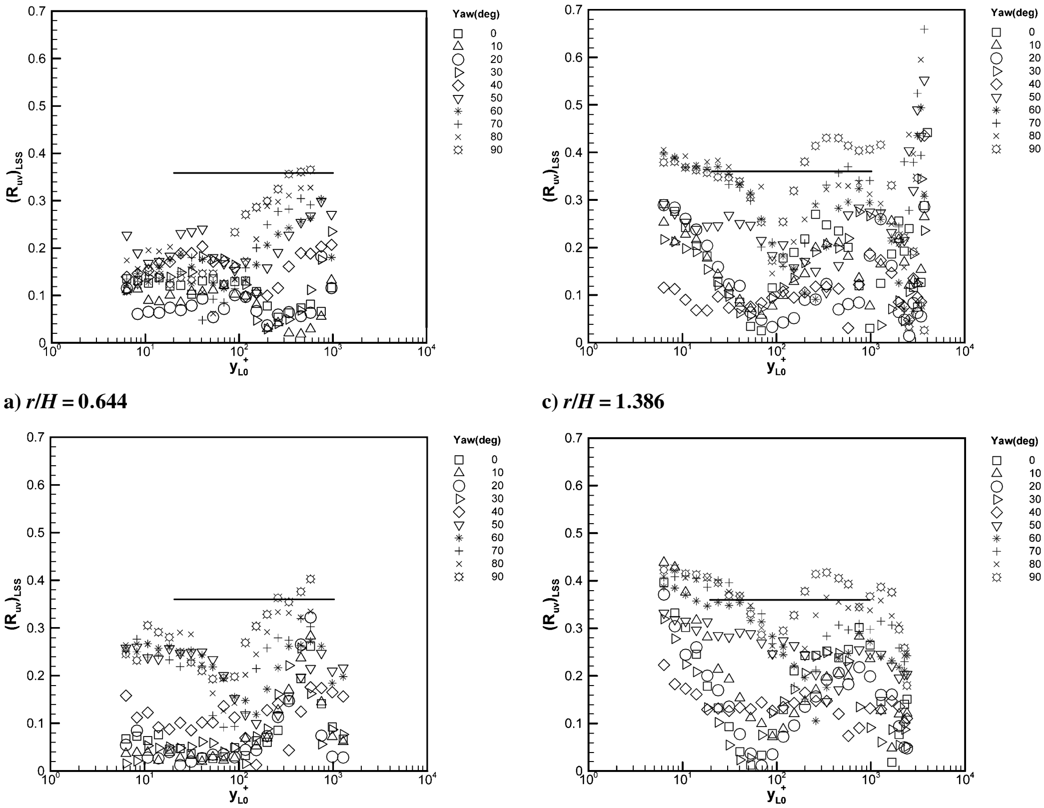

a) $r/H = 0.644$

c) $r/H = 1.386$

b) $r/H = 0.91$

d) $r/H = 1.615$

Fig. 10 R_{uv} in local shear stress coordinates: ——, two-dimensional TBL level over middle region.

two-dimensional TBL for $r/H \geq 0.781$ and reaches the local minimum at $y^+_{L0} \approx 100$ because of strong three-dimensional flows with vortices that are generated by the pressure gradient and spiral around the focus. For $\psi \geq 50$ deg, $1/S$ is relatively high in these layers due to higher Reynolds shearing stresses for $y^+_{L0} < 100$ and $\overline{v^2}$ is lower for $y^+_{L0} > 100$. For $0 \leq \psi \leq 40$ deg, in these layers the numerator in $1/S$, the Reynolds shearing stress magnitude, is much lower downstream from the separation because of the lower production rates in the backflow zone. It does not change much up to $y^+_{L0} \approx 100$ downstream of the separation and begins to increase significantly above this height within $0 \leq \psi \leq 40$ deg because of the higher production rates due to the higher Reynolds normal stress and positive velocity gradient in the backflow region for $y^+_{L0} > 100$. It shows higher values in this region from $y^+_{L0} \approx 456$, where the saddle–focus structure disappears, than for $\psi \geq 50$ deg. Although not presented here, the Townsend's structural parameter $A1 \equiv [(-\overline{uv_L})^2 + (-\overline{vw_L})^2]^{0.5}/q^2$ vs y^+_{L0} in local coordinates shows very similar behavior to $1/S$. It is the ratio of the magnitude between Reynolds shearing stress and 2TKE ($u^2 + v^2 + w^2$, in which u, v, and w are mean quantities). It is approximately 0.1–0.13 for $70 \leq y^+ \leq 1000$ in a two-dimensional TBL, although some inactive motions contribute to the TKE through $\overline{u^2}$. The $A1$ has much lower value and a local minimum at about $y^+_{L0} \approx 100$ within $0 \leq \psi \leq 40$ deg than for $\psi \geq 50$ deg for $r/H \geq 0.91$.

Figure 10 shows the correlation coefficient between u'_{LSS} and v'_{LSS}, $(R_{uv})_{\mathrm{LSS}} \equiv -\overline{uv_{\mathrm{LSS}}}/\sqrt{u^2_{\mathrm{LSS}}}\sqrt{v^2_{\mathrm{LSS}}}$, in local shear stress (LSS) coordinates in which there is $-\overline{vw_{\mathrm{LSS}}} = 0$. It is also less correlated and has a lower local minimum, less than 0.1, at around $y^+_{L0} \approx 80$–100 within $0 \leq \psi \leq 40$ deg than for $\psi \geq 50$ deg for $r/H \geq 0.91$. From these three parameters, there is less correlation between u'_L and v'_L and lower Reynolds shearing stress generated by the rotational motions with respect to v^2_L in the saddle and focus structure region than in a two-dimensional TBL. However, the TKE relative to the magnitude of the Reynolds shearing stress is higher than in a two-dimensional TBL. The $-\overline{uw_L}$ is more significant than $-\overline{vw_L}$ in this region, which means that u'_L and w'_L are more correlated than v'_L and w'_L.

A general explanation for low $1/S$, $A1$, and $(R_{uv})_{\mathrm{LSS}}$ values can be given for regions where the mean flow angle, $\tan^{-1}(\overline{W_L}/\overline{U_L})$, varies with the distance from the wall, y^+_{L0}. The turbulent flow at different y^+_{L0} comes from different directions and is not well correlated with the turbulence at other y^+_{L0}. Thus, the correlation coefficients and the Reynolds shearing stresses are low, whereas the skewed eddies out of the x_L–y_L plane generate significant $-\overline{uw_L}$, which is one of the major indicators for three dimensionality.

Bimodal Histogram, Skewness, and Flatness Factors

There are bimodal velocity probability histograms in U_L and W_L in local coordinates. Double peak histograms in U_L appear downstream of $r/H = 0.841$, a little upstream from the saddle separation, and are significant along the centerline. Bimodal histograms in W_L appear from downstream from the saddle separation in $10 \leq \psi \leq 30$ deg as well as in U_L. Figure 11 shows bimodal histograms of U_L, V_L, and W_L at specific locations. The V_L has no bimodal feature.

In this region, velocity fluctuations are switched between two dominant peak values so that the flow is highly unsteady and may be meandering with a low frequency. Figure 12 shows the contour of the joint probability density function of U_L and W_L, $P(U_L, W_L)$, at $r/H = 1.386$, $\psi = 30$ deg, and $y^+_{L0} = 261$, which is close to the focus. A 50×50 bin grid was used. There are also two dominant contour level peaks that show very high correlations between u' and w'. It also suggests that the focus location may move sequentially in the x_L–z_L plane. The spectrum analysis of w'_L around the focus (not presented here) using the slotted correlation function[18] shows very low-frequency peaks of approximately $fH/U_{\mathrm{ref}} \approx 0.01$.

To investigate the effect of bimodality of U_L and W_L on higher-order structure functions, the skewness and flatness factors are examined. Figure 13 shows the skewness factor, $(S_u)_L \equiv u^3_L/(u^2_L)^{3/2}$, and the flatness factor, $(F_u)_L \equiv u^4_L/(u^2_L)^2$, along the centerline downstream of separation. They are 0 and 3, respectively, for a Gaussian distribution. Near the wall, all locations are positively skewed and

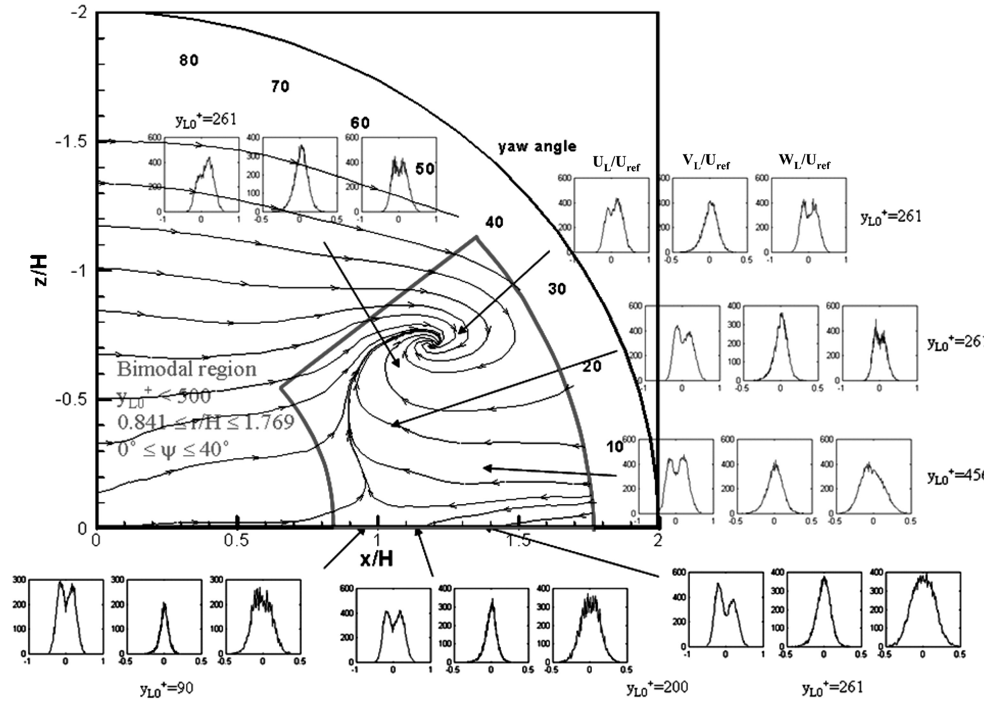

Fig. 11 Bimodal histograms of U_L, V_L, and W_L in local coordinates.

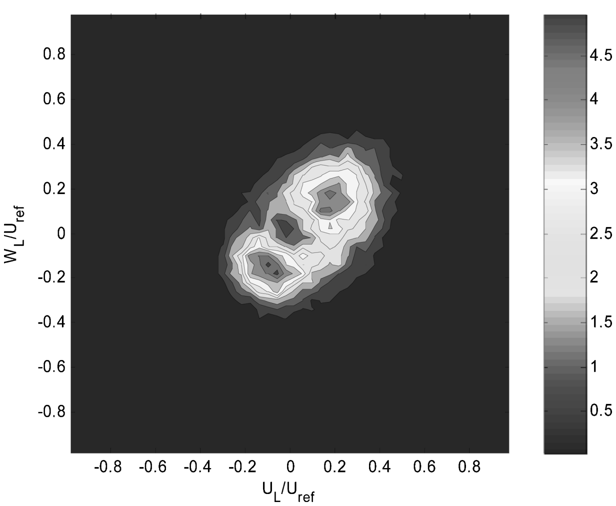

Fig. 12 Joint probability density function of U_L and W_L in local coordinates at center of focus separation, $r/H = 1.386$, $\psi = 30$ deg, and $y_{L0}^+ = 261$; $\int_{-\infty}^{\infty}\int_{-\infty}^{\infty} p(U_L, W_L)\, dU_L\, dW_L = 1$.

the skewness increases farther downstream as well as away from the wall. It has a local maximum of approximately $y_{L0}^+ \approx 100$. The local minimum of $\overline{U_L}$ appears very close to this location. The almost symmetric bimodal histograms appear where the skewness changes its sign and the flatness shows a local minimum at this height. In the case of symmetric double peaks in a histogram, there are relatively infrequent dominant amplitude fluctuations so that the edges in the probability histogram are a smaller fraction as compared to nonbimodal histograms. Closer to the wall than y_{L0}^+ for $(S_u)_L \approx 0$, the skewness increases positively because one peak in the positive fluctuation is reduced, and, consequently, this edge is larger. This increases the flatness too. Similarly, farther than y_{L0}^+ for $(S_u)_L \approx 0$, the skewness decreases up to $y_{L0}^+ \approx 500$–600, but the flatness increases from its local minimum value because of larger negative edge. There are no bimodal features further than this height, and

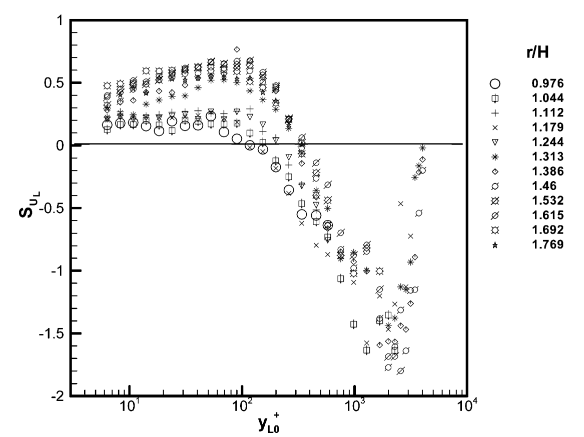

a) Skewness factor

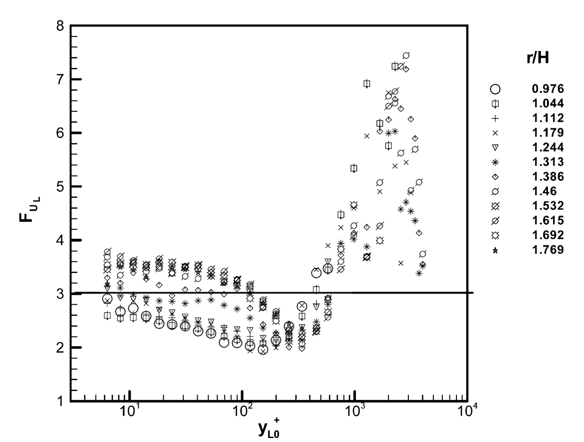

b) Flatness factor

Fig. 13 Skewness and flatness factor of U_L downstream from separation along centerline in local coordinates: ——, Gaussian distribution factors.

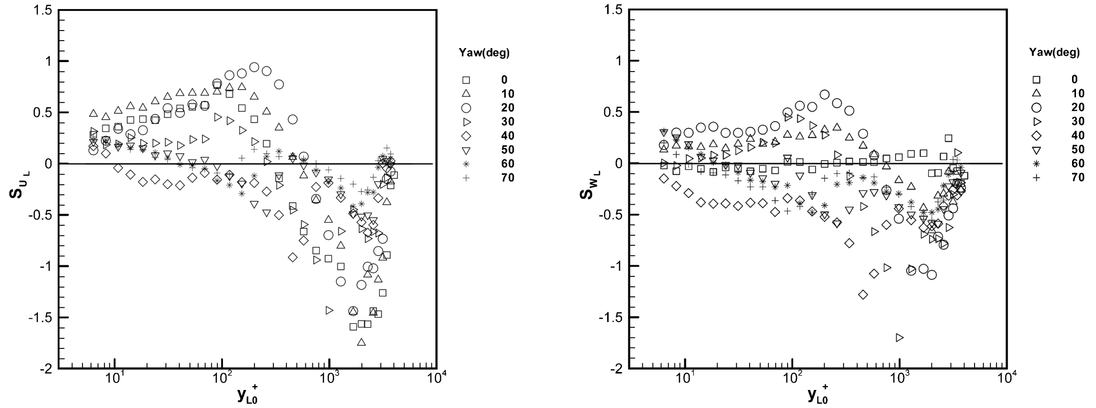

a) U_L b) W_L

Fig. 14 Skewness factor of U_L and W_L along $r/H = 1.386$ in local coordinates: ——, Gaussian distribution factors.

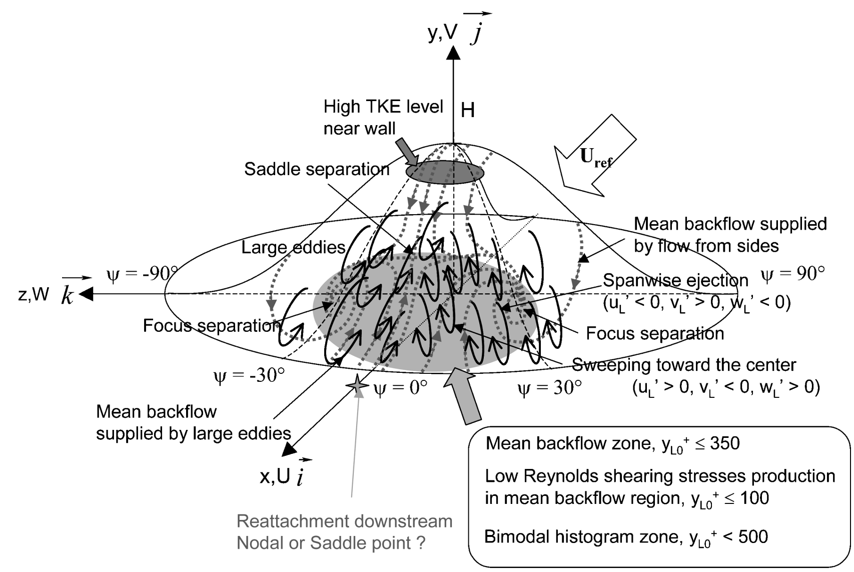

Fig. 15 Flow structures on leeside of bump: black, large eddies; - - - -, near surface flow patterns; and gray, mean backflow zone.

the skewness and the flatness have very high negative values due to occasional large-magnitude negative fluctuations generated by the large-eddy ejection motions, $u_L' < 0$ and $v_L' > 0$. In the overlap region, the skewness factors change the sign and the flatness factors are small. The $\overline{uv}_L$ values are large negatives in this region. This shows that the intense mixing occurs with smaller amplitude but with a much higher probability of fluctuations.

Figure 14 shows the skewness factors of U_L and W_L, $(S_w)_L \equiv w_L^3/(w_L^2)^{3/2}$, along $r/H = 1.386$ in local coordinates. The focus is located at approximately $r/H = 1.386$ and $\psi = 30$ deg. The $(S_w)_L$ is very close to zero for $\psi = 0$ deg. The $(S_u)_L$ and $(S_w)_L$ show similar trends for $10 \leq \psi \leq 30$ deg, where they have relatively high positive values up to $y_{L0}^+ \approx 400$. They increase away from the surface, and the largest positive skewness appears at $y_{L0}^+ \approx 200$ for $\psi = 20$ deg in both U_L and W_L. This means that there are large-amplitude sweeping motions, $u_L' > 0$ and $v_L' < 0$, toward the center, $w_L' > 0$, up to $y_{L0}^+ \approx 400$ for $10 \leq \psi \leq 30$ deg. Above this height, the motions decrease negatively in both U_L and W_L, which means that large-amplitude spanwise ejection motions, $u_L' < 0$ and $v_L' > 0$, with $w_L' < 0$. For $\psi \geq 40$ deg, the skewness decreases to negative values as the height moves from the near wall. Figure 15 shows flow features in the leeside of bump.

V. Conclusions

Fine-spatial-resolution three-velocity-component LDV measurements are presented for the TBL over the leeside of an axisymmetric bump. Mean velocities, Reynolds stresses, and all triple products have been measured from the nearest bump surface. They show a saddle-type three-dimensional separation at $x/H \approx 0.96$ on the centerline of the bump. The downstream backflow and the streamwise flow from upstream of the saddle separation spread spanwise and generate one focus separation on each side at $x/H \approx 1.2$ and $z/H \approx \pm 0.7$. The saddle-focus separated flow is not only on the nearest wall surface, but also extends up to $y_{L0}^+ \approx 340$. In the mean backflow region within $0 \leq \psi \leq 30$ deg, more TKE is generated than Reynolds shearing stresses in local coordinates because u_L' and v_L' are less correlated and w_L' is correlated much stronger with u_L' than with v_L'. The large eddies and the flow from the bump side supplies the mean backflow. Because $(\gamma_{pU})_L$ is never zero, the large eddies supply the intermittently forward flow in this mean backflow region, similar to a two-dimensional separated TBL. Bimodal probability distributions of U_L and W_L appear in this region due to the unsteady and low-frequency meandering of the flowfield. These bimodal features may represent the unsteady separation patterns such as switching between detached and attached flows. Significant symmetric bimodal histograms make the histogram edges smaller, so that they occur with close to zero skewness and minimum flatness factors.

Compared with experiments, Davidson and Dahlström's[9] hybrid LES–unsteady RANS calculations show only one counterclockwise rotating positive streamwise vortex in a negative z/H side at a wake plane, even though the vortex center is closer toward the centerline than the measured vortex center. Their mean flow at the wall separates from about $x/H \approx 1$ on the centerline, which is very close to the measured location. However, it has a weaker focus separation, making a narrower spiral zone. On the other hand, the Wang et al.[7]

NLEV RANS results for skin-friction lines agree better with the presented data than Davidson and Dahlström's calculations. However, the saddle separation occurs far upstream, and there is a clockwise rotating negative streamwise vortex in a negative z/H side at wake planes in their models. The Temmerman et al.[8] LES calculations for a 10-times-lower-Reynolds-number flow shows similar results to the Wang et al.[7] results, except at a much higher TKE level in the separated flow downstream than the RANS models. Also, their RANS and LES calculations show a much thicker mean backflow region downstream in the center plane up to $x/H \approx 3.5$. Therefore, the entire flow structures over this bump need to be better modeled.

As mentioned earlier, the LDV measurements show only one saddle and two foci mean separation points on the bump surface. It is expected that there is an attachment point on the centerline downstream. If this attachment point is nodal, as suggested by earlier oilflows,[5,10] then two saddle separation points must be present downstream to satisfy the kinematical rules.[2] However, if there is a saddle reattachment point along the centerline, as suggested by the CFD calculations, then no additional separation points are needed to satisfy the kinematics. Therefore, to get complete flow features over this bump, measurements are needed for this attachment and separation region downstream.

Acknowledgments

This work was supported by the U.S. Office of Naval Research Under N00014-01-1-0421, L. P. Purtell and Ronald Joslin, Program Managers. The authors appreciate the interactions with S. Menon, M. A. Leschziner, and L. Davidson and their colleagues. The LabView-based three-dimensional laser Doppler velocimetry processor used for measurements was developed by Todd Lowe.

References

[1]Delery, J. M., "Physics of Vortical Flows," *AIAA Journal*, Vol. 29, No. 5, 1992, pp. 856–876.

[2]Hunt, J. C. R., Abell, C. J., Peterka, J. A., and Woo, H., "Kinematical Studies of the Flows Around Free or Surface-Mounted Obstacles; Applying Topology to Flow Visualization," *Journal of Fluid Mechanics*, Vol. 86, Pt. 1, 1978, pp. 179–200.

[3]Tobak, M., and Peake, D. J., "Topology of Three-Dimensional Separated Flows," *Annual Review of Fluid Mechanics*, Vol. 14, 1982, pp. 61–85.

[4]Fureby, C., Alin, N., Wikström, N., Menon, S., Svanstedt, N., and Perrson, L., "Large-Eddy Simulation of High-Reynolds-Number Wall-Bounded Flows," *AIAA Journal*, Vol. 42, No. 3, 2004, pp. 457–468.

[5]Simpson, R. L., Long, C. H., and Byun, G., "Study of Vortical Separation from an Axisymmetric Hill," *International Journal of Heat and Fluid Flow*, Vol. 23, No. 5, 2002, pp. 582–591.

[6]Patel, N., Stone, C., and Menon, S., "Large-Eddy Simulation of Turbulent Flow over an Axisymmetric Hill," AIAA Paper 03-0967, Jan. 2003.

[7]Wang, C., Jang, Y. J., and Leschziner, M. A., "Modelling Two- and Three-Dimensional Separation from Curved Surfaces with Anisotropy-Resolving Turbulence Closures," *International Journal of Heat and Fluid Flow*, Vol. 25, No. 3, 2004, pp. 499–512.

[8]Temmerman, L., Wang, C., and Leschziner, M. A., "A Comparative Study of Separation from a Three-Dimensional Hill Using LES and Second-Moment-Closure RANS Modeling," European Community on Computational Methods in Applied Sciences, 4th European Congress on Computational Methods in Applied Sciences and Engineering, Jyväskylä, Finland, July 2004.

[9]Davidson, L., and Dahlström, S., "Hybrid LES-RANS: Computation of the Flow Around a Three-Dimensional Hill," European Research Community on Flow, Turbulence and Combustion, International Symposium on Engineering Turbulence Modelling and Measurements, Sardinia, Italy, May 2005.

[10]Byun, G., Simpson, R. L., and Long, C. H., "Study of Vortical Separation from Three-Dimensional Symmetric Bumps," *AIAA Journal*, Vol. 42, No. 4, 2004, pp. 754–765.

[11]Tian, Q., Simpson, R. L., and Tang, G., "Flow Visualization on the Linear Compressor Cascade Endwall Using Oil Flows and Laser Doppler Anemometry," *Measurement Science and Technology*, Vol. 15, No. 9, 2004, pp. 1910–1916.

[12]Byun, G., Ölçmen, M. S., and Simpson, R. L., "A Miniature Laser-Doppler Velocimeter for Simultaneous Three-Velocity-Component Measurements," *Measurement Science and Technology*, Vol. 15, No. 10, 2004, pp. 2075–2082.

[13]Ölçmen, M. S., Simpson, R. L., and George, J., "Some Reynolds Number Effects on Two- and Three-Dimensional Turbulent Boundary Layers," *Experiments in Fluids*, Vol. 31, No. 2, 2001, pp. 219–228.

[14]Ölçmen, M. S., and Simpson, R. L., "A Five-Velocity-Component Laser-Doppler Velocimeter for Measurements of a Three-Dimensional Turbulent Boundary Layer," *Measurement Science and Technology*, Vol. 6, No. 6, 1995, pp. 702–716.

[15]Schumann, U., "Realizability of Reynolds Stress Turbulent Model," *Physics of Fluids*, Vol. 20, No. 5, 1977, pp. 721–725.

[16]Simpson, R. L., "Turbulent Boundary Layer Separation," *Annual Review of Fluid Mechanics*, Vol. 21, 1989, pp. 205–234.

[17]Ölçmen, M. S., and Simpson, R. L., "An Experimental Study of a Three-Dimensional Pressure-Driven Turbulence Boundary Layer," *Journal of Fluid Mechanics*, Vol. 290, 1995, pp. 225–262.

[18]Nobach, H., "Local Time Estimation for the Slotted Correlation Function of Randomly Sampled LDA Data," *Experiments in Fluids*, Vol. 32, No. 3, 2002, pp. 337–345.

J. Gore
Associate Editor